
PIBNET: A PHYSICS-INSPIRED BOUNDARY NETWORK FOR MULTIPLE SCATTERING SIMULATIONS

Rémi Marsal

U2IS, ENSTA

Institut Polytechnique de Paris

remi.marsal@ensta.fr

Stéphanie Chaillat

Laboratoire POEMS, CNRS, INRIA, ENSTA

Institut Polytechnique de Paris

stephanie.chaillat@ensta.fr

ABSTRACT

The boundary element method (BEM) provides an efficient numerical framework for solving multiple scattering problems in unbounded homogeneous domains, since it reduces the discretization to the domain boundaries, thereby condensing the computational complexity. The procedure first consists in determining the solution trace on the boundaries of the domain by solving a boundary integral equation, after which the volumetric solution can be recovered at low computational cost with a boundary integral representation. As the first step of the BEM represents the main computational bottleneck, we introduce PIBNet, a learning-based approach designed to approximate the solution trace. The method leverages a physics-inspired graph-based strategy to model obstacles and their long-range interactions efficiently. Then, we introduce a novel multiscale graph neural network architecture for simulating the multiple scattering. To train and evaluate our network, we present a benchmark consisting of several datasets of different types of multiple scattering problems. The results indicate that our approach not only surpasses existing state-of-the-art learning-based methods on the considered tasks but also exhibits superior generalization to settings with an increased number of obstacles. github.com/ENSTA-U2IS-AI/pibnet

1 INTRODUCTION

Multiple scattering is defined by Martin (2006) as "the interaction of fields with two or more obstacles", as illustrated in fig. 1. The main challenge in such problems lies in the combined effect of the number of obstacles and their separation distances, as these factors govern the complexity of the multiple reflections. The boundary element method (BEM) (Bonnet, 1999) is an efficient numerical method for solving linear partial differential equations (PDEs) such as the one involved in multiple scattering. Unlike the finite element method (FEM), the BEM reformulates the PDE into a boundary integral equation (BIE) with unknowns restricted to the problem boundaries. After solving the BIE, the solution in the volumetric domain is evaluated using the boundary integral representation. Thus, by reducing the dimensionality of the problem, the BEM can offer significant gains in computational efficiency and accuracy compared to the FEM for wave propagation problems in unbounded domains. Within the BEM, the two computational stages have very different costs: solving the BIE on the boundaries is significantly more expensive than evaluating the boundary integral representation to recover the volumetric solution.

To reduce the overall computational cost, several learning-based approaches have been proposed to simulate multiple scattering (Hao et al., 2021; Nair et al., 2025). Taking advantage of the recent development in neural network architectures for solving PDEs, these approaches rely either on discretizing the solution domain or on neural fields. Discretization-based methods (Pfaff et al., 2020; Zhdanov et al., 2025) handle complex geometries and boundary conditions but inherit the computational cost of traditional solvers. Neural field approaches (Raissi et al., 2019) represent the solution as a continuous function, allowing inference at arbitrary points, but for complex geometries, they still rely on conditioning over discretized domains (Serrano et al., 2024; Alkin et al., 2024; 2025). Due to these limitations, learning-based multiple-scattering methods have been restrained to two-dimensional problems only.

Inspired by methods based on the BEM that learn the boundary solution instead of solving the BIE to alleviate the BEM bottleneck (Lin et al., 2021; Fang et al., 2024), we propose, PIBNet. It is a learning-based method to simulate PDEs that can be solved with the BEM i.e. linear and semi-linear PDEs. More specifically, in this paper, we address multiple scattering due the inherent challenges of such problems. We first present a benchmark including simulation datasets that focus on 3D exterior scattering problems for both Helmholtz and Laplace problems under Dirichlet or Neumann boundary conditions, as well as meaningful metrics to evaluate the estimated solution. Neural fields, which have frequently been used to solve similar tasks (Lin et al., 2021; Fang et al., 2024), are not suitable here due to the presence of multiple disjoint obstacles. Since efficiently capturing long-range interactions between obstacles is crucial, a natural approach is to explore transformer-based methods developed for solving PDEs or point cloud processing. However, as shown numerically in section 6.2, these approaches exhibit limited performance. To improve the accuracy, we propose PIBNet, a method in which distant interactions are explicitly represented as edges in graphs. To avoid the computational cost of adding all possible interaction edges, we propose a physics-informed strategy for connecting distant points, combined with a U-Net-style multi-scale graph neural network (GNN) based on MeshGraphNet (Fortunato et al., 2022) that approximate the boundary solution to multiple scattering problems. This approach outperforms existing state-of-the-art learning-based methods dedicated to solving PDEs. Finally, we show the ability of our architecture to generalize to environments with up to three times more obstacles than those seen in the training set. In summary, we propose the following contributions:

1. A benchmark of datasets of exterior Laplace and Helmholtz problems with multiple disjoint obstacles obtained using the BEM.
2. PIBNet, our method that combines a physics-inspired strategy for modeling long-range interactions as graphs and a new multiscale GNN architecture for estimating the boundary solution of the multiple scattering problems.

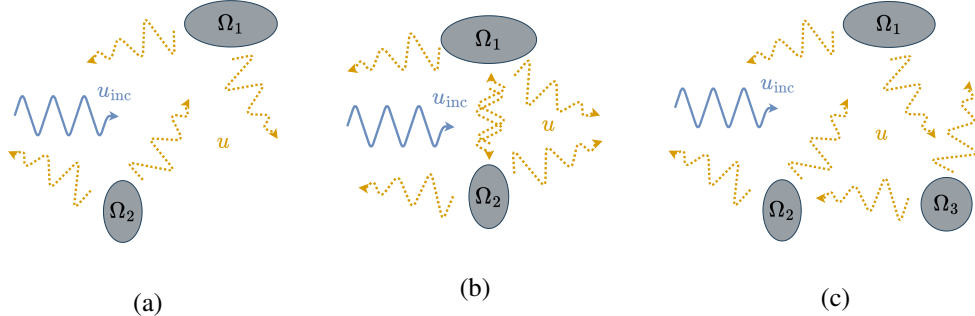


Figure 1: Illustrations of the resulting field u (dashed arrows) from the scattering of an incoming wave u_{inc} (solid arrows) by two obstacles Ω_1 and Ω_2 (a). In (b), the obstacles are closer to each other and in (c), there is a third obstacle Ω_3 . This induces more complex interactions between u_{inc} and obstacles.

2 PRELIMINARIES ON THE BOUNDARY ELEMENT METHOD

This section provides a comprehensive overview of the boundary element method (BEM) (Bonnet, 1999) through the problem of multiple scattering (Martin, 2006) of an incident wave u_{inc} . Let $\Omega = \bigcup_{i=1}^n \Omega_i \in \mathbb{R}^3$ be the union of n closed bounded sets Ω_i , $1 \leq i \leq n$, representing obstacles that do not intersect. We assume that each set Ω_i has a Lipschitz-continuous and piecewise-smooth boundary Γ_i and let $\Gamma = \bigcup_{i=1}^n \Gamma_i$. The homogeneous Helmholtz equation is given by:

$$\begin{cases} \mathcal{L}u = 0 & \text{in } \mathbb{R}^3 \setminus \Omega \\ u = -u_{\text{inc}} & \text{on } \Gamma \end{cases} \quad (1)$$

where $\mathcal{L} = \Delta + k^2$ with k the wavenumber. We assume the Sommerfeld radiation condition: $\lim_{|\mathbf{x}| \rightarrow \infty} |\mathbf{x}| \left(\frac{\partial}{\partial |\mathbf{x}|} - ik \right) u(\mathbf{x}) = 0$ is satisfied, which ensures that no energy is radiated from infinity. Therefore, the total field is given by $u_{\text{tot}} = u + u_{\text{inc}}$.

The BEM relies on a reformulation of eq. (1) as a boundary integral equation. The key ingredient in this reformulation is the Green's function G , defined as the solution of $\mathcal{L}G = \delta$ where δ denotes the Dirac delta function. For our problem, the variational form of the boundary integral equation can be defined as follows:

$$\int_{\Gamma} u(\mathbf{x})q(\mathbf{x})d\mathbf{x} = \int_{\Gamma \times \Gamma} G(\mathbf{x} - \mathbf{y})q(\mathbf{x})p(\mathbf{y})d\mathbf{x}d\mathbf{y} \quad (2)$$

where q is a test function and p is the unknown. The solution of this equation gives only the trace of the density p . The second step of the method consists in applying the boundary integral representation to compute the scattered field in the volume:

$$u(\mathbf{x}) = \mathcal{S}(p)(\mathbf{x}), \quad \mathbf{x} \in \mathbb{R}^3 \setminus \Omega \quad (3)$$

where $\mathcal{S}(p)(\mathbf{x}) = \int_{\Gamma} G(\mathbf{x} - \mathbf{y})p(\mathbf{y})d\mathbf{y}$ is the single layer potential operator.

After discretization of Γ , eq. (2) becomes a fully populated linear system, with storage and solution complexities of $O(N^2)$ and $O(N^3)$, respectively. Instead of direct solvers, iterative solvers such as GMRES (Saad & Schultz, 1986) are often employed for BIEs. The number of iterations needed for convergence provides insight into the intrinsic difficulty of the problem, such as the level of multiple scattering occurring between obstacles in the given configurations. Fast algorithms like the Fast Multipole Method or Hierarchical Matrices (Chaillat et al., 2008; 2017; Darve, 2000) bring the complexity of BEM down to linear or quasi-linear, yet the method remains computationally expensive for parametric investigations involving many configurations or frequency ranges.

The computational bottleneck of the BEM lies in solving the boundary integral equation. Once the solution trace on the boundary is obtained, the volumetric field can be efficiently reconstructed using the boundary integral representation. We develop a machine learning model to predict the boundary solution, allowing us to accelerate the most expensive part of the computation while still recovering the full volumetric solution.

3 RELATED WORK

3.1 LEARNING AND BOUNDARY ELEMENT METHOD

Many approaches aim to replace the resolution of the BIE with a neural network, since it is the most computationally demanding part of the BEM. Most of these approaches are conditional neural fields (Lin et al., 2021; 2023; Qu et al., 2024). In these models, the inputs consist of 2D coordinates of points on the surface, together with additional information specific to the problem, such as surface shape parameters or boundary conditions. To improve accuracy, Fang et al. (2024) and Meng et al. (2024) use a frequency representation for input values with a high variation range. More complex geometries have also been addressed with GNN in Wang et al. (2025b). Once the solution of the BIE is returned by the neural network, it can be used to compute the solution of the original PDE with the boundary integral representation as in BEMs. Thus, learning-based BEM can provide an efficient framework for solving PDEs since the solution domain dimension of the BIE is smaller than that of the original PDE. However, all the approaches discussed in this section are limited to problems involving a single surface. This work addresses scattering problems with multiple disjoint obstacles, a setting that introduces interesting challenges.

3.2 LEARNING PDES ON UNSTRUCTURED DATA

PDEs often require processing unstructured data, either because of complex domains (airfoils, geological formations) or to leverage adaptive meshing (Pfaff et al., 2020). Computer-vision-based approaches that are effective with grid-structured data (Wang et al., 2025a; Colagrande et al., 2025) can be adapted to unstructured data with continuous convolutions (Ummenhofer et al., 2019), for

instance. Other works (Li et al., 2023a;b) project the unstructured data onto a regular grid in the latent space before applying FNO layers (Li et al., 2021). As mentioned in the previous section, neural fields may be leveraged (Fang et al., 2024) but they are limited by the capacity of the conditioning mechanism to address complex geometries. Many GNN approaches have been developed (Sanchez-Gonzalez et al., 2020; Li et al., 2019; 2020a;b). One of the most popular, MeshGraphNet (Pfaff et al., 2020), has been extended several times to handle multiple resolutions (Fortunato et al., 2022; Cao et al., 2023; Ripken et al., 2023). However, none of these approaches expand latent dimensions for low-resolution meshes. Following U-Net (Ronneberger et al., 2015), the multi-level extension of MeshGraphNet we propose in this paper implements this feature. More recently, multiple transformer-based methods reach top performance on numerous benchmarks, most of which focusing on reducing the quadratic computation complexity of attention. Thus, several approaches propose efficient attention mechanisms (Li et al., 2022; Hao et al., 2023; Xiao et al., 2024). Other approaches propose to apply transformers locally. For instance, the Transolver architecture (Li et al., 2022; Luo et al., 2025) performs attention on learnable slices of flexible shape of the input data. Erwin (Zhdanov et al., 2025) and GOAT (Wen et al., 2025) clustered the input data in hierarchical balls. Finally, as shown in (Zhdanov et al., 2025), attention-based point cloud processing approaches (Wu et al., 2024b) may be relevant for learning PDEs with unstructured data. In this paper, based on our knowledge of the BEM, we propose a neural architecture to approximate the boundary solution of multiple scattering problems that outperforms other learning-based approaches designed for solving PDEs on unstructured data.

4 DATASETS & METRICS

This section presents the benchmark employed for solving the following three problems:

1. Exterior Helmholtz Dirichlet problem with an incident wave of unit amplitude emitted from a monopole source. The Dirichlet boundary condition is therefore parametrized by the source location $\mathbf{x}_0 \in \mathbb{R}^3 \setminus \Omega \cup \Gamma$ and the wavenumber k :

$$u(\mathbf{x}) = -\frac{e^{ik\|\mathbf{x}-\mathbf{x}_0\|_2}}{\|\mathbf{x}-\mathbf{x}_0\|_2}, \quad \mathbf{x} \in \Gamma. \quad (4)$$

2. Exterior Helmholtz Neumann problem with an incident unit plane wave. The Neumann boundary condition is parametrized by the incident wave's direction \mathbf{v} and the wavenumber k :

$$\frac{\partial u}{\partial \mathbf{n}} = -ik e^{ik\mathbf{x}\cdot\mathbf{v}}, \quad \mathbf{x} \in \Gamma \quad (5)$$

where $\frac{\partial u}{\partial \mathbf{n}} = \nabla u(\mathbf{x}) \cdot \mathbf{n}$ is the normal derivative and \mathbf{n} the normal vector to Γ at \mathbf{x} .

3. Exterior Laplace Dirichlet problem with standard boundary conditions:

$$u(\mathbf{x}) = -\Phi_0 - \frac{\Phi_1}{\|\mathbf{x}-\mathbf{x}_0\|_2} - 2\Phi_2 \mathbf{v} \cdot \frac{\mathbf{x}-\mathbf{x}_0}{\|\mathbf{x}-\mathbf{x}_0\|_2}, \quad \mathbf{x} \in \Gamma \quad (6)$$

where Φ_0 , Φ_1 and Φ_2 are three constants between -1 and 1 , $\mathbf{x}_0 \in \mathbb{R}^3 \setminus \Omega \cup \Gamma$ and \mathbf{v} is a unit vector in \mathbb{R}^3 .

We generated a training dataset and several test datasets for each problem. Each sample consists of randomly sized and positioned, non-overlapping ellipsoidal obstacles, randomly selected boundary condition parameters, and the corresponding boundary solution trace as the label. Ellipsoids are characterized by their center coordinates and semi-axis lengths.

For each problem, the training set samples contain three obstacles, and we created a test set with three obstacles. Moreover, for Laplace and Helmholtz Dirichlet problems, we also provide test sets with six and nine obstacles. The meshes representing the obstacles and the trace solution were generated using the BEMPP library (Betcke & Scroggs, 2021). We also recorded the number of GMRES iterations required to converge for each sample to monitor their computational complexity. Further details about the datasets are provided in table 1, and the BIE formulations used to generate the labels are included in the appendix (see section A).

For evaluation, we assess the performance on the Laplace problem using the relative error of the trace, Err_{rel} . For the Helmholtz problems, we introduce two metrics: the relative error of the trace

Table 1: Main characteristics of our datasets. Lengths are given without unit.

Number of samples in the training / test sets	Environment size	Edges length in obstacle meshes	Ellipses semi-axes length (min - max)	Wavelength (min - max)
$10^4 / 10^3$	$10 \times 10 \times 10$	0.1	0.3 - 1.5	0.6 - 6

amplitude, Err_{ampl} , and the absolute error of the trace phase, $\text{Err}_{\text{angle}}$. The definitions of these metrics for a single sample are given by:

$$\text{Err}_{\text{rel}} = \sum_{x \in \Gamma} |\hat{p}(x) - p^*(x)| / (\sum_{x \in \Gamma} |p^*(x)|) \quad (7)$$

$$\text{Err}_{\text{ampl}} = \frac{1}{\#\Gamma} \sum_{x \in \Gamma} \left| \frac{|\hat{p}(x)| - |p^*(x)|}{|p^*(x)|} \right| \quad (8)$$

$$\text{Err}_{\text{angle}} = \frac{1}{\#\Gamma} \sum_{x \in \Gamma} \text{atan2}(\sin(\Delta p), \cos(\Delta p)), \quad \Delta p = \angle \hat{p}(x) - \angle p^*(x) \quad (9)$$

where p^* and \hat{p} denote the ground-truth boundary trace obtained from the BEM and the neural network prediction, respectively, $\#$ indicates the cardinality of a set, and \angle stands for the angle of a complex number. These metrics are then averaged over all samples in a dataset.

5 METHOD

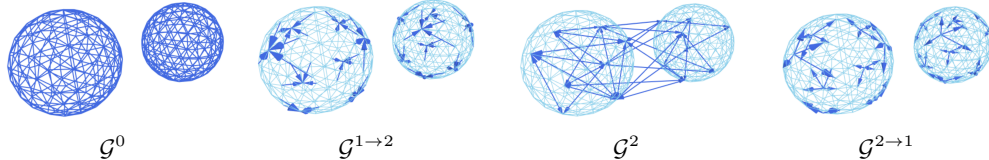


Figure 2: Illustration of some directed graph representations used in PIBNet in the case of two obstacles. Graph edges are in dark blue, while the light blue corresponds to the obstacle meshes. \mathcal{G}^0 : the *boundary graph* (arrows have been omitted for readability), $\mathcal{G}^{1 \rightarrow 2}$: the *downsampling graph* from level 1 to 2, \mathcal{G}^2 : the *distant nodes graph* and $\mathcal{G}^{2 \rightarrow 1}$: the *upsampling graph* from level 2 to 1. We omit the downsampling and upsampling graphs $\mathcal{G}^{0 \rightarrow 1}$ and $\mathcal{G}^{1 \rightarrow 0}$ between levels 0 and 1 which are similar to graphs $\mathcal{G}^{1 \rightarrow 2}$ and $\mathcal{G}^{2 \rightarrow 1}$ at a lower resolution.

This paper focuses on the task of multiple scattering which addresses the interaction of a field with several obstacles Martin (2006). Therefore, an accurate representation of the obstacles and of their precise relative position is mandatory. For this purpose, we build graphs representing the obstacles at various resolution levels and graphs for the transitions between two levels. At the highest level (i.e. the lowest resolution), we create a graph connecting distant obstacles with a physics-inspired edge selection strategy. In this section, we present our PIBNet method: after defining the different graphs and the physics-inspired edge selection strategy, we introduce our GNN architecture which consists of an encoder and a processor. The encoder initializes the graph nodes and edges features, while the processor updates these features to model the interactions between the obstacles.

Graphs definition Let $\mathcal{G}^0 = (V^0, E^0)$ be the graph called *boundary graph* with nodes V^0 and bidirected edges E^0 that corresponds to the union of the n meshes $\mathcal{G}_{\Gamma_i}^0 = (V_{\Gamma_i}^0, E_{\Gamma_i}^0)$ that represents the discretized boundaries Γ_i of the obstacles Ω_i , $1 \leq i \leq n$, so that $\mathcal{G}^0 = \bigcup_{i=1}^n \mathcal{G}_{\Gamma_i}^0 = (\bigcup_{i=1}^n V_{\Gamma_i}^0, \bigcup_{i=1}^n E_{\Gamma_i}^0)$. We build a multiscale representation of \mathcal{G}^0 with L levels using an octree so that for each level $0 < j < L$, we have a new set of nodes V^j satisfying $p(V^j) \subset p(V^{j-1})$ where $p(V)$ returns the set of positions of the nodes in the node set V . We also obtain downsampling directed edges $E^{j-1 \rightarrow j}$ and upsampling directed edges $E^{j \rightarrow j-1}$ that link nodes between level $j-1$ and j . The downsampling edges are used to create *downsampling graphs*

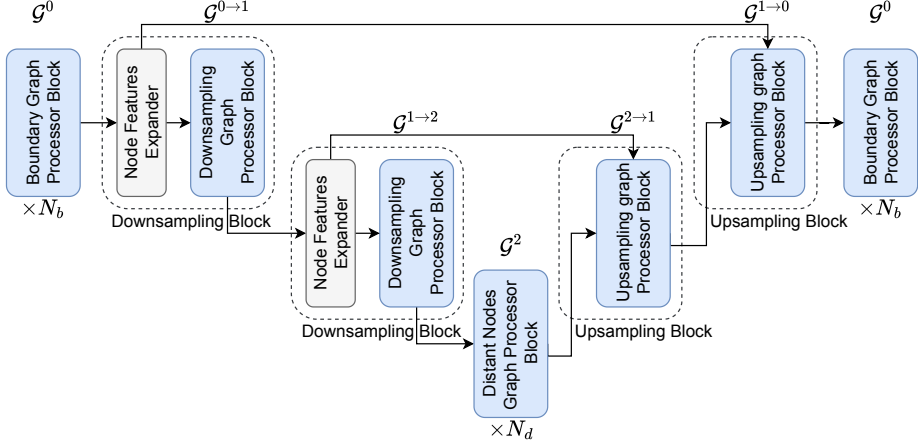


Figure 3: Illustration of the processor part of PIBNet GNN architecture with a number of levels $L = 3$. The graph representation used by each processor block is given above the corresponding block. It is composed of N_b Boundary Graph Processor Blocks at the beginning, then 2 Downsampling Blocks, N_d Distant Nodes Graph Processor Blocks, $L - 1$ Upsampling Blocks, and N_b Boundary Graph Processor Blocks at the end.

$\mathcal{G}^{j-1 \rightarrow j} = (V^{d,j-1}, E^{j-1 \rightarrow j})$ where $p(V^{d,j}) = p(V^j)$ while the upsampling edges provides *upsampling graphs* $\mathcal{G}^{j \rightarrow j-1} = (V^{u,j-1}, E^{j \rightarrow j-1})$ where $p(V^{u,j}) = p(V^j)$. To model the interactions between distant nodes, we create a *distant nodes graph* $\mathcal{G}^{L-1} = (V^{L-1}, E^{L-1})$ with bidirected edges E^{L-1} so that each nodes of the highest level V^{L-1} is connected to a fraction α of the other nodes in V^{L-1} according to a physics-inspired strategy described below. We illustrated some of these graphs in fig. 2.

Physics-inspired edge selection strategy In this paper, we address the Laplace and Dirichlet problems, for which the Green functions are given by $G(\mathbf{x}) = -\frac{1}{4\pi r}$ and $G(\mathbf{x}) = -\frac{e^{-ikr}}{4\pi r}$, respectively, where $r = \|\mathbf{x}\|_2$, $\mathbf{x} \in \mathbb{R}^3 \setminus \Omega \cup \Gamma$. This implies that obstacles interact more strongly at short distances, while long-range interactions remain present. Thus, to generate the edges E^{L-1} in the *distant nodes graph* \mathcal{G}^{L-1} , we propose an edge selection strategy consistent with physics that favors connections between close nodes but still allows some longer-range interactions. For each of the $\alpha|V^{L-1}|$ required edges originating from a node in V^{L-1} , n_c candidate edges are randomly proposed from the $V^{L-1} - 1$ potential candidates, and the shortest one is chosen.

Encoder The encoder initializes the edge features of each graph and the node features of \mathcal{G}^0 ; the node features of the other graphs are initialized later. The edge features of each graph are encoded using a dedicated MLP. Thus, for each edge e of a graph \mathcal{G} , the inputs of the encoder are a sinusoidal positional encoding of the distance $D(e)$ between the two connected nodes, the normalized direction of e , and other features which depend on the boundary conditions (more details in section B). The output dimension is d^0 for edges in E^0 , d^j for edges in $E^{j-1 \rightarrow j}$ and $E^{j-1 \rightarrow j}$, and d^{L-1} for edges in E^{L-1} . The node features of V^0 are encoded with an MLP whose inputs are determined by the boundary conditions (more details in section B). The output dimension of this MLP is d^0 .

Processor The processor, illustrated in fig. 3, is composed of multiple processor blocks that are applied to a graph $\mathcal{G} = (V, E)$. Each processor blocks consists of one edge feature update eq. (10) followed by one node feature update eq. (11):

$$f'_{e_{kl}} = \phi^e(f_{e_{kl}}, f_{v_k}, f_{v_l}) \quad (10)$$

$$f'_{v_k} = \phi^n(f_{v_k}, \sum_k f'_{e_{kl}}) \quad (11)$$

where ϕ^e and ϕ^n are MLPs and $f_{e_{kl}}$ are the features of edge $e_{kl} \in E$ connecting node $v_k \in V$ to node $v_l \in V$ of features f_{v_k} and f_{v_l} , respectively.

The first step of the processor consists of N_b processor blocks applied to the boundary graph \mathcal{G}^0 . It is followed by $L - 1$ downsampling blocks, each applied to a downsampling graph $\mathcal{G}^{j-1 \rightarrow j}$, $0 < j < L$. To this end, the features of nodes $V^{d,j-1}$ are initialized by the node features expander, which is an MLP that projects the node features of $V^{d,j-1}$ (or of V^0 when $j = 0$) from a dimension d^{j-1} to a dimension d^j , before a processor block is applied. Then, the node features of V^{L-1} are initialized with the output node features of the final downsampling block and N_d processor blocks are applied to the distant nodes graph \mathcal{G}^{L-1} . Thereafter, $L - 1$ upsampling blocks are applied, one to each upsampling graph $\mathcal{G}^{j \rightarrow j-1}$, that is composed of a processor block that reduces the feature dimension from d^j to d^{j-1} . The node features of $V^{u,j-1}$ are initialized with the node features of $V^{u,j}$ (or V^{L-1} if $j = L - 1$) for the nodes that exist in both sets and with the node features of $V^{d,j-1}$ otherwise. Finally, N_b processor blocks are applied to the graph \mathcal{G}^0 whose node features are initialized with the node features of $V^{u,1}$, output by the last upsampling block. The last processor block returns an output vector of dimension d^f for each node in V^0 which corresponds to the approximate BIE solution on the discretization of the boundary Γ . For the Laplace problem $d^f = 1$ and for the Helmholtz problem $d^f = 2$ corresponding to the real and imaginary parts of the BIE solution, respectively.

6 EXPERIMENTS

We evaluate PIBNet through extensive experiments on the new benchmark proposed. We compare the results of our method against those of other state-of-the-art learning-based approaches for solving PDEs on unstructured data such as MeshGraphNet (Pfaff et al., 2020) Transolver (Wu et al., 2024a), Transolver++ (Luo et al., 2025) and Erwin (Zhdanov et al., 2025). We also include the point cloud processing method Point Transformer v3 referred to as PTv3 (Wu et al., 2024b) in our comparisons.

6.1 IMPLEMENTATION DETAILS

Regarding our architecture, we set the number of levels to $L = 3$ and we connect each node to a fraction $\alpha = 0.1$ of the other nodes at the highest level $L - 1$. The expansion rate of the dimension of latent layers is 2 when the level index increases by one. This means that for $0 < j < L$, the dimension d^j of a latent layer is given by $d^j = d^0 \times 2^j$. Moreover, we set the dimension of the latent layers of the first level to $d^0 = 64$. We perform the octree using Ripken et al. (2023) implementation and keeping every two levels. In the physics-inspired strategy, the number of candidate edges n_c per required edge in E^{L-1} is set to 2 unless otherwise mentioned. The architecture details of the methods we compare against are given in section C. All models are supervised with the groundtruth solution of the BIE using a Huber loss (Huber, 1992) with parameter $\delta = 1.0$. The models are trained from scratch for 100 epochs, with AdamW optimizer (Loshchilov & Hutter, 2017), a batch size of 16, a learning rate starting at 10^{-4} decreasing to 10^{-7} with a cosine scheduler, and gradient clipping by norm with a maximum value of 1.0. We also leverage data augmentation which consists of the same random rotation applied to the node positions of the input mesh and to the source location. Hardware details are given in section D.

6.2 RESULTS

Table 2: Benchmark results on three obstacle datasets.

Method	Number of Parameters (M)	Laplace Err _{rel}	Helmholtz Err _{ampl}	Dirichlet Err _{angle}	Helmholtz Err _{ampl}	Neumann Err _{angle}
MeshGraphNet	2.4	0.197	0.286	0.191	0.071	0.072
PTv3	77.2	0.066	0.148	0.141	0.065	0.068
Transolver	4.6	0.183	0.596	0.454	0.070	0.073
Transolver++	4.2	0.195	0.635	0.466	0.103	0.122
Erwin	7.9	0.119	0.218	0.175	0.074	0.076
Ours	5.2	0.041	0.091	0.090	0.046	0.047

In table 2, we present performance on the test datasets with the same data distribution as the training set, i.e., with three obstacles per sample. Since our approach involves random processes, we report the mean of five evaluations, each with a different seed. We measure an average relative standard

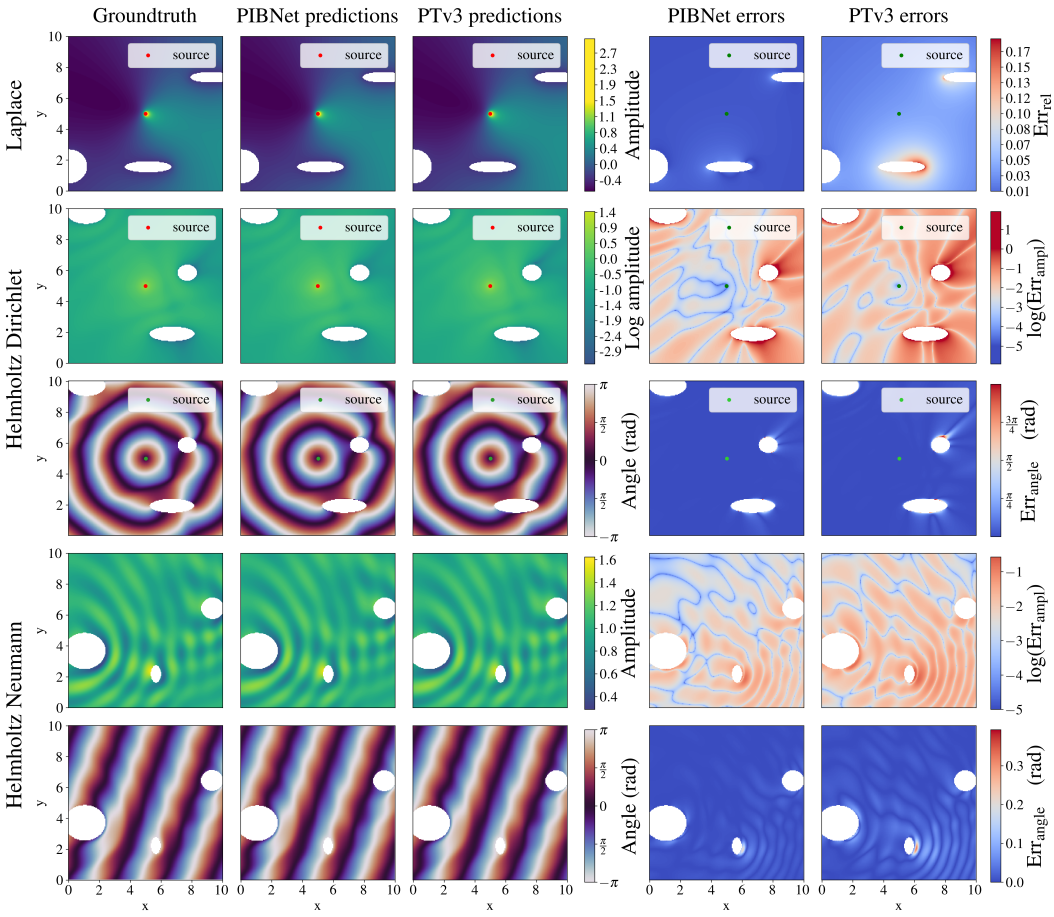


Figure 4: Qualitative results for the three problems of our benchmark with three obstacles (in white). From left to right are the 3D volumetric solution of the total field obtained with GMRES (the groundtruth), with PIBNet and with PTv3 predictions of the trace solution, respectively, and the corresponding errors relative to the groundtruth with PIBNet and PTv3, respectively. For each problem, the 3D volumetric solutions of the total field and their associated errors are sampled within a square domain of side length 10 on the plane $z = 0$.

deviation of 0.3% across all datasets and metrics, demonstrating the stability and reproducibility of our method. The results highlight the superiority of PIBNet over the other relevant state-of-the-art approaches showing an average improvement of 32% across the different metrics and datasets relative to the second best approach PTv3 (Wu et al., 2024b). This may be due to the better expressiveness of our graph-based representation, which explicitly models distant interactions with edges, compared to multihead attention. PTv3 good performance may stem from its larger number of parameters, but it may also be attributed to its architecture specifically designed for processing point clouds. The irregular distribution of points in point cloud datasets aligns more closely with our data, which consists of points sampled on the surface of distant objects. In contrast, PDE benchmarks (Pfaff et al., 2020; Janny et al., 2023) are typically based on nearly regular meshes that cover almost the entire domain. We also note that Transolver (Wu et al., 2024a) and Transolver++ (Luo et al., 2025) are not adapted for this task since they reach lower performance than MeshGraphNet which is applied to the raw obstacle meshes so it cannot model interactions between obstacles. In section E, we analyze the correlation between the per-sample mean absolute error and the GMRES iteration count (a proxy for the number of reflections), the wavenumber and the dispersion of obstacles. Qualitative results for the two top methods on our benchmark, PIBNet and PTv3, are shown in fig. 4.

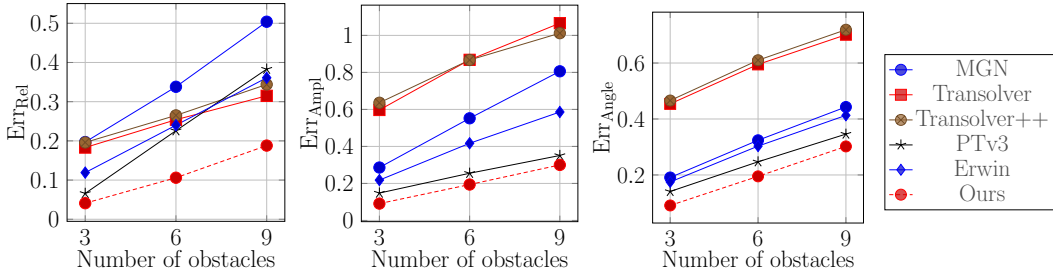


Figure 5: Estimation errors as a function of the number of obstacles for the Laplace Dirichlet problem (left) and the Helmholtz Dirichlet problem (middle and right).

6.3 GENERALIZATION

In fig. 5, we examine the generalization ability of models trained on datasets with three obstacles per sample to test environments with six and nine obstacles. As the number of obstacles exceeds three, we adapt the physics-inspired edge selection strategy during inference to adjust the focus on the closest obstacles. Specifically, the number n_c of candidate edges per required edge in E^{L-1} is increased to 3. A thorough study of the impact of n_c on performance for different numbers of obstacles is provided in section F. The results show a consistent decline in performance across all methods as the number of obstacles increases. This trend is expected because a higher number of obstacles induces quadratic growth in pairwise interactions. This substantially increases the problem’s complexity, leading to reduced performance in scenarios with six or nine obstacles. Additionally, our models are only trained with a fixed number of obstacles per dataset sample, which may affect their ability to generalize to a different number of obstacles. Despite the decrease in performance as the number of obstacles increases, these results demonstrate that our PIBNet method generalizes better than the other methods considered.

6.4 RUNTIME ANALYSIS

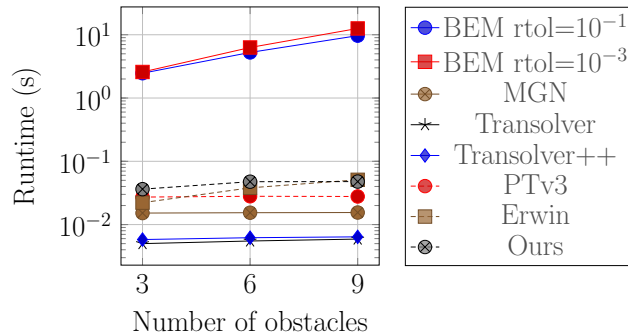


Figure 6: Comparison of runtime on with respect to the number of obstacles for learning-based methods and for the BEM considering different different convergence tolerance thresholds rtol for GMRES.

In fig. 6, we study the runtime for generating the trace of the solution on the boundaries for the Helmholtz Dirichlet problem with respect to the number of obstacles. We compare approaches running on the same GPU including learning-based methods and the BEM with different convergence tolerance thresholds rtol for GMRES. This study shows that learning-based approaches are orders of magnitude faster than the BEM. However, unlike learning-based methods, whose runtime depends only on the number of nodes in the obstacle meshes, the BEM’s runtime is sensitive to wavelength and the relative position of obstacles. Regarding learning-based methods, the very low runtime of Transolver and Transolver++ reflects minimal computational cost, as both approaches are designed to process very large meshes (Wu et al., 2024a; Luo et al., 2025), which explains their limited performance. PIBNet has the highest runtime for three- and six-obstacle problems, but remains close

to Point Transformer V3 and Erwin. However, we observe that PIBNet scales better than Erwin, which has the worst runtime for nine-obstacle problems.

6.5 ABLATION

In table 3, we study the impact of the different components of our method for the exterior Helmholtz Dirichlet problem. First, we highlight the importance of connecting distant nodes to account for dependencies between them. Then, we demonstrate the advantages of using a U-Net-like multi-level architecture with an optimal number of levels, which is achieved with $L = 3$. To be fair in terms of computational complexity, we maintain the same number of edges connecting distant nodes as the number of levels varies. We justify that expanding the dimension of the latent layers at each level results in better performance than keeping it constant even if the average latent dimension is identical. Finally, we show that our physics-inspired edge selection strategy for connecting nodes at the highest level is superior to a purely random edge selection.

Table 3: Ablation study. n_c corresponds to the number of candidate edges per required edge in E^{L-1} .

Distant nodes connection	Number of levels L	Latent dimension at the finest level	Latent dimension expansion factor	n_c	Err _{ampl}	Err _{angle}
✗	1	64	—	—	0.328	0.205
✓	1	64	—	1	0.202	0.181
✓	2	64	2	1	0.138	0.135
✓	3	64	2	1	0.097	0.097
✓	4	64	2	1	0.115	0.112
✓	3	128	1	1	0.112	0.110
✓	3	64	2	2	0.091	0.090
✓	3	64	2	3	0.093	0.092

7 CONCLUSION

In this work, we introduce PIBNet, a new learning-based method for solving linear and semi-linear PDEs that can be solved by the BEM and focus on multiple scattering problems. This approach proposes to explicitly represent distant interactions that occur in such tasks using graphs created with a physics-inspired strategy. Based on the BEM, we present a new multiscale GNN architecture for estimating the solution trace on the boundary of the domain. Thus, the solution for the entire domain can be quickly estimated using the boundary integral representation of the problem. To evaluate this method, we introduce a novel benchmark of multiple scattering simulations which includes Laplace and Helmholtz problems. Our results demonstrate that PIBNet surpasses other state-of-the-art learning-based methods for solving PDEs and processing point clouds. Additionally, PIBNet generalizes better to settings with a greater number of obstacles.

REFERENCES

- Benedikt Alkin, Andreas Fürst, Simon Schmid, Lukas Gruber, Markus Holzleitner, and Johannes Brandstetter. Universal physics transformers: A framework for efficiently scaling neural operators. *Advances in Neural Information Processing Systems*, 37:25152–25194, 2024.
- Benedikt Alkin, Maurits Bleeker, Richard Kurle, Tobias Kronlachner, Reinhard Sonnleitner, Matthias Dorfer, and Johannes Brandstetter. Ab-up: Scaling neural cfd surrogates for high-fidelity automotive aerodynamics simulations via anchored-branched universal physics transformers. *arXiv preprint arXiv:2502.09692*, 2025.
- Timo Betcke and Matthew W. Scroggs. Bempp-cl: A fast Python based just-in-time compiling boundary element library. *Journal of Open Source Software*, 6(59):2879, March 2021. doi: 10.21105/joss.02879.
- Marc Bonnet. *Boundary Integral Equation Methods for Solids and Fluids*. John Wiley & Sons, 1999.

-
- Yadi Cao, Menglei Chai, Minchen Li, and Chenfanfu Jiang. Efficient learning of mesh-based physical simulation with bi-stride multi-scale graph neural network. In *International conference on machine learning*, pp. 3541–3558. PMLR, 2023.
- S. Chaillat, M. Bonnet, and J.-F. Semblat. A multi-level fast multipole BEM for 3-d elastodynamics in the frequency domain. *Computer Methods in Applied Mechanics and Engineering*, 197:4233–4249, 2008. doi: 10.1016/j.cma.2008.04.018.
- S. Chaillat, L. Desiderio, and P. Ciarlet. Theory and implementation of h-matrix based iterative and direct solvers for helmholtz and elastodynamic oscillatory kernels. *Journal of Computational Physics*, 351:165–186, 2017. doi: 10.1016/j.jcp.2017.08.021.
- Alex Colagrande, Paul Caillon, Eva Feillet, and Alexandre Allauzen. Linear attention with global context: A multipole attention mechanism for vision and physics. *arXiv preprint arXiv:2507.02748*, 2025.
- Tri Dao, Dan Fu, Stefano Ermon, Atri Rudra, and Christopher Ré. Flashattention: Fast and memory-efficient exact attention with io-awareness. *Advances in neural information processing systems*, 35: 16344–16359, 2022.
- Éric Darve. The fast multipole method: Numerical implementation. *Journal of Computational Physics*, 160(1):195–240, 2000. doi: 10.1006/jcph.2000.6451. URL <https://www.sciencedirect.com/science/article/pii/S0021999100964519>.
- Zhiwei Fang, Sifan Wang, and Paris Perdikaris. Learning only on boundaries: A physics-informed neural operator for solving parametric partial differential equations in complex geometries. *Neural computation*, 36(3):475–498, 2024.
- Meire Fortunato, Tobias Pfaff, Peter Wirnsberger, Alexander Pritzel, and Peter Battaglia. Multiscale meshgraphnets. *ICML-AI4Science*, 2022.
- Wenqu Hao, Yongpin P Chen, Pei-Yao Chen, Ming Jiang, Sheng Sun, and Jun Hu. Solving two-dimensional scattering from multiple dielectric cylinders by artificial neural network accelerated numerical green’s function. *IEEE Antennas and Wireless Propagation Letters*, 20(5):783–787, 2021.
- Zhongkai Hao, Zhengyi Wang, Hang Su, Chengyang Ying, Yinpeng Dong, Songming Liu, Ze Cheng, Jian Song, and Jun Zhu. Gnot: A general neural operator transformer for operator learning. In *International Conference on Machine Learning*, pp. 12556–12569. PMLR, 2023.
- Peter J Huber. Robust estimation of a location parameter. In *Breakthroughs in statistics: Methodology and distribution*, pp. 492–518. Springer, 1992.
- Steeven Janny, Aurélien Beneteau, Madiha Nadri, Julie Digne, Nicolas Thome, and Christian Wolf. Eagle: Large-scale learning of turbulent fluid dynamics with mesh transformers. *ICLR*, 2023.
- Yunzhu Li, Jiajun Wu, Russ Tedrake, Joshua B Tenenbaum, and Antonio Torralba. Learning particle dynamics for manipulating rigid bodies, deformable objects, and fluids. *ICLR*, 2019.
- Zijie Li, Kazem Meidani, and Amir Barati Farimani. Transformer for partial differential equations’ operator learning. *Transactions on Machine Learning Research*, 2022.
- Zongyi Li, Nikola Kovachki, Kamyar Azizzadenesheli, Burigede Liu, Kaushik Bhattacharya, Andrew Stuart, and Anima Anandkumar. Neural operator: Graph kernel network for partial differential equations. *ICLR Workshop DeepDiffEq*, 2020a.
- Zongyi Li, Nikola Kovachki, Kamyar Azizzadenesheli, Burigede Liu, Andrew Stuart, Kaushik Bhattacharya, and Anima Anandkumar. Multipole graph neural operator for parametric partial differential equations. *Advances in Neural Information Processing Systems*, 33:6755–6766, 2020b.
- Zongyi Li, Nikola Kovachki, Kamyar Azizzadenesheli, Burigede Liu, Kaushik Bhattacharya, Andrew Stuart, and Anima Anandkumar. Fourier neural operator for parametric partial differential equations. *ICLR*, 2021.

-
- Zongyi Li, Daniel Zhengyu Huang, Burigede Liu, and Anima Anandkumar. Fourier neural operator with learned deformations for pdes on general geometries. *Journal of Machine Learning Research*, 24(388):1–26, 2023a.
- Zongyi Li, Nikola Kovachki, Chris Choy, Boyi Li, Jean Kossaifi, Shourya Otta, Mohammad Amin Nabian, Maximilian Stadler, Christian Hundt, Kamyar Azizzadenesheli, et al. Geometry-informed neural operator for large-scale 3d pdes. *Advances in Neural Information Processing Systems*, 36: 35836–35854, 2023b.
- Guochang Lin, Pipi Hu, Fukai Chen, Xiang Chen, Junqing Chen, Jun Wang, and Zuoqiang Shi. Binet: learning to solve partial differential equations with boundary integral networks. *CSIAM Transactions on Applied Mathematics*, 2021.
- Guochang Lin, Fukai Chen, Pipi Hu, Xiang Chen, Junqing Chen, Jun Wang, and Zuoqiang Shi. Bi-greennet: learning green’s functions by boundary integral network. *Communications in Mathematics and Statistics*, 11(1):103–129, 2023.
- Ilya Loshchilov and Frank Hutter. Decoupled weight decay regularization. *International Conference on Learning Representations (ICLR)*, 2017.
- Huakun Luo, Haixu Wu, Hang Zhou, Lanxiang Xing, Yichen Di, Jianmin Wang, and Mingsheng Long. Transolver++: An accurate neural solver for pdes on million-scale geometries. *ICML*, 2025.
- P. A. Martin. *Multiple Scattering: Interaction of Time-Harmonic Waves with N Obstacles*, volume 107 of *Encyclopedia of Mathematics and its Applications*. Cambridge University Press, 2006.
- Bin Meng, Yutong Lu, and Ying Jiang. Solving partial differential equations in different domains by operator learning method based on boundary integral equations. *arXiv preprint arXiv:2406.02298*, 2024.
- Siddharth Nair, Timothy F Walsh, Greg Pickrell, and Fabio Semperlotti. Multiple scattering simulation via physics-informed neural networks. *Engineering with Computers*, 41(1):31–50, 2025.
- Tobias Pfaff, Meire Fortunato, Alvaro Sanchez-Gonzalez, and Peter Battaglia. Learning mesh-based simulation with graph networks. In *International conference on learning representations*, 2020.
- Wenzhen Qu, Yan Gu, Shengdong Zhao, Fajie Wang, and Ji Lin. Boundary integrated neural networks and code for acoustic radiation and scattering. *International Journal of Mechanical System Dynamics*, 4(2):131–141, 2024.
- Maziar Raissi, Paris Perdikaris, and George E Karniadakis. Physics-informed neural networks: A deep learning framework for solving forward and inverse problems involving nonlinear partial differential equations. *Journal of Computational physics*, 2019.
- Winfried Ripken, Lisa Coiffard, Felix Pieper, and Sebastian Dziadzio. Multiscale neural operators for solving time-independent pdes. *NeurIPS workshop DLDE III*, 2023.
- Olaf Ronneberger, Philipp Fischer, and Thomas Brox. U-net: Convolutional networks for biomedical image segmentation. In *International Conference on Medical image computing and computer-assisted intervention*, pp. 234–241. Springer, 2015.
- Youcef Saad and Martin H Schultz. Gmres: A generalized minimal residual algorithm for solving nonsymmetric linear systems. *SIAM Journal on scientific and statistical computing*, 7(3):856–869, 1986.
- Alvaro Sanchez-Gonzalez, Jonathan Godwin, Tobias Pfaff, Rex Ying, Jure Leskovec, and Peter Battaglia. Learning to simulate complex physics with graph networks. In *International conference on machine learning*, pp. 8459–8468. PMLR, 2020.
- Louis Serrano, Thomas X Wang, Etienne Le Naour, Jean-Noël Vitta, and Patrick Gallinari. Aroma: Preserving spatial structure for latent pde modeling with local neural fields. *Advances in Neural Information Processing Systems*, 37:13489–13521, 2024.

-
- Benjamin Ummenhofer, Lukas Prantl, Nils Thuerey, and Vladlen Koltun. Lagrangian fluid simulation with continuous convolutions. In *International conference on learning representations*, 2019.
- Sifan Wang, Jacob H Seidman, Shyam Sankaran, Hanwen Wang, George J Pappas, and Paris Perdikaris. Cvit: Continuous vision transformer for operator learning. *ICLR*, 2025a.
- Taiyi A Wang, Ian McBrearty, and Paul Segall. Graph neural network based elastic deformation emulators for magmatic reservoirs of complex geometries. *Volcanica*, 8(1):95–109, 2025b.
- Shizheng Wen, Arsh Kumbhat, Levi Lingsch, Sepehr Mousavi, Yizhou Zhao, Praveen Chandrashekhar, and Siddhartha Mishra. Geometry aware operator transformer as an efficient and accurate neural surrogate for pdes on arbitrary domains. *arXiv preprint arXiv:2505.18781*, 2025.
- Haixu Wu, Huakun Luo, Haowen Wang, Jianmin Wang, and Mingsheng Long. Transolver: A fast transformer solver for pdes on general geometries. *ICML*, 2024a.
- Xiaoyang Wu, Li Jiang, Peng-Shuai Wang, Zhijian Liu, Xihui Liu, Yu Qiao, Wanli Ouyang, Tong He, and Hengshuang Zhao. Point transformer v3: Simpler faster stronger. In *Proceedings of the IEEE/CVF conference on computer vision and pattern recognition*, pp. 4840–4851, 2024b.
- Zipeng Xiao, Zhongkai Hao, Bokai Lin, Zhijie Deng, and Hang Su. Improved operator learning by orthogonal attention. *ICML*, 2024.
- Maksim Zhdanov, Max Welling, and Jan-Willem van de Meent. Erwin: A tree-based hierarchical transformer for large-scale physical systems. *ICML*, 2025.

APPENDIX

A DATASETS DETAILS

The BIE and the representation formulations used for each problem we address are given in table 4. The BIE solution is approximated with GMRES (Saad & Schultz, 1986) with a convergence tolerance of 10^{-5} .

Table 4: Formulations of the BIE and of the representations used to generate the dataset for each problem where S and N are the single-layer and the hypersingular boundary integral operator, respectively, while \mathcal{S} and \mathcal{D} are the single-layer and the double-layer potential operator, respectively.

Problem	BIE	Representation
Laplace Dirichlet	$Sp = u$	$u = \mathcal{S}p$
Helmholtz Dirichlet	$Sp = u$	$u = \mathcal{S}p$
Helmholtz Neumann	$Np = \frac{\partial u}{\partial n}$	$u = \mathcal{D}p$

B INPUT DETAILS

Laplace Dirichlet problem

- Node encoder inputs:
 - A sinusoidal positional encoding of the distance between the current node and x_0 ,
 - The normalized direction of x_0 relative to the current node,
 - The normalized direction v ,
 - Each term of the boundary condition computed at the current node position.
- Edge encoder inputs:
 - A sinusoidal positional encoding of the length of the edge,
 - The normalized direction of the edge,

Helmholtz Dirichlet problem

- Node encoder inputs:
 - A sinusoidal positional encoding of the distance between the current node and the source \mathbf{x}_0 ,
 - The normalized direction of the source \mathbf{x}_0 relative to the current node,
 - The wavenumber of the sample,
 - The sine and the cosine of the angle of an incident wave coming from \mathbf{x}_0 .
- Edge encoder inputs:
 - A sinusoidal positional encoding of the length of the edge,
 - The normalized direction of the edge,
 - The wavenumber of the sample,
 - The sine and the cosine of the angle of an incident wave at the destination node coming from the source node.

Helmholtz Neumann problem

- Node encoder inputs:
 - The normalized direction of \mathbf{v} of the incident wave,
 - The wavenumber of the sample,
 - The sine and the cosine of the angle of the incident wave at the location of the node,
 - A sinusoidal positional encoding of the distance between the current node and the average of node positions,
 - The direction of the average of the node positions.
- Edge encoder inputs:
 - A sinusoidal positional encoding of the length of the edge,
 - The normalized direction of the edge,
 - The wavenumber of the sample,
 - The sine and the cosine of the angle of an incident wave at the destination node coming from the source node.

Here, the use of average node positions is mandatory for methods that are not based on meshes to provide information about node positions relative to each other. For the other problems, this information comes from the distance and direction of the source \mathbf{x}_0 . For the sake of fairness, this input is used with all methods.

C IMPLEMENTATION DETAILS

The implementation details of the different state-of-the-art methods we compare against are given in table 5.

D HARDWARE DETAILS

The data was generated on a 36 Intel Core i9-10980XE (3.00GHz) CPUs with double precision and a tolerance threshold for GMRES set to $\text{rtol} = 10^{-5}$ to obtain a highly accurate groundtruth. The time required to generate our training datasets with 10000 samples depends on the problem and the BIE formulation. Generating the Laplace Dirichlet, Helmholtz Dirichlet and Helmholtz Neumann training datasets took 12, 36 and 96 hours, respectively. All training experiments have been conducted on a single NVIDIA RTX 3090 GPU with 24GB memory. Training times range from 3-4 hours for Point Transformer v3, the later benefiting from flash attention acceleration Dao et al. (2022), to more than 18 hours for Transolver and Transolver++ because of gradient accumulation which is mandatory when the batch size exceeds 1. Otherwise, training time is 8-10 hours for PIBNet, 10-11 hours for MeshGraphNet and 12 hours for Erwin. Note that flash attention cannot be used for training Erwin as its distance-based attention bias position encoding is mandatory to achieve good performance.

Table 5: Implementation details of the different methods we compare against in this paper. The hyperparameters have been tuned to maximize performance on the Helmholtz Dirichlet problem.

Model	Parameter	Value
MeshGraphNet (Pfaff et al., 2020)	Processor depth	15
	Latent dimension	128
Point Transformer V3 (Wu et al., 2024b)	Grid Size	0.2
	Latent dimensions	(64, 128, 256, 512)
	Window sizes	(512, 512, 512)
	Encoder depths	(2, 2, 2, 6)
	Encoder heads	(4, 8, 16, 32)
	Encoder patch size	1024
	Decoder depths	(2, 2, 2)
	Decoder heads	(4, 8, 16)
	Decoder patch size	1024
Transolver (Wu et al., 2024a)	Stride	2
	Latent dimension	256
	Number of layers	8
Transolver++ (Luo et al., 2025)	MPL ratio	4
	Latent dimension	256
	Number of layers	8
Erwin (Zhdanov et al., 2025)	MPL ratio	4
	MPNN dim.	64
	Latent dimensions	(64, 128, 256)
	Window sizes	(512, 512, 512)
	Encoder depths	(2, 2, 6)
	Encoder heads	(4, 8, 16)
	Decoder depths	(2, 2)
	Decoder heads	(4, 8)
	Stride	2
	Distance-based attention bias	Enabled

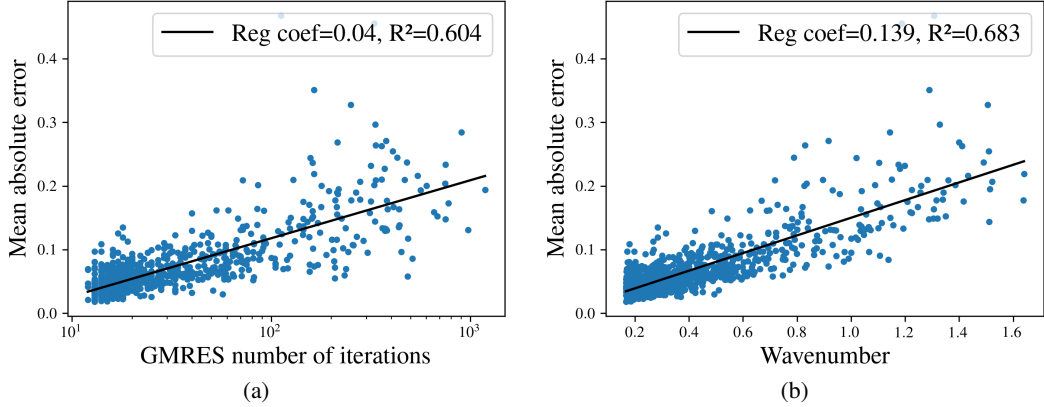
E ANALYSIS OF THE MODEL PERFORMANCE

In this section, we examine how the performance varies with respect to the number of GMRES iterations, the wavenumber and the obstacle dispersion for each dataset sample.

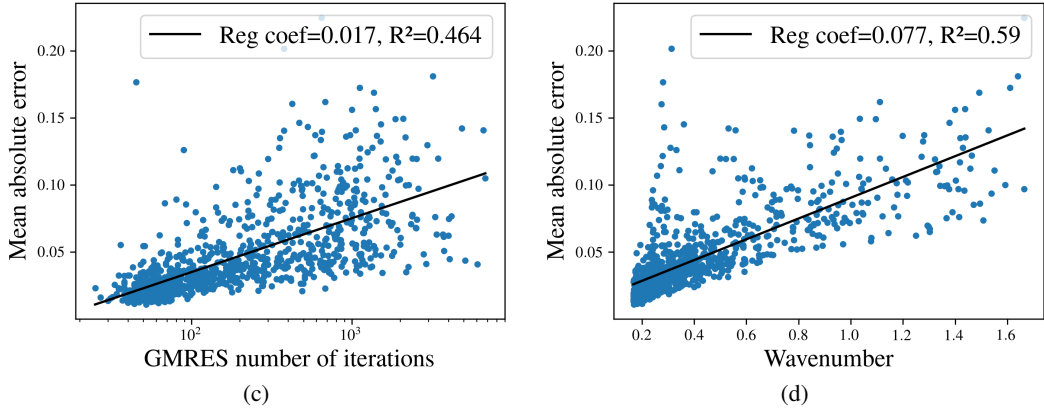
For wave propagation problems, we expect the number of GMRES iterations to reflect the difficulty of the problem, i.e., the number of reflections between obstacles. Consequently, we predict that PIBNet will have more difficulty with this case, which is indeed what we observe in fig. 7 (a, c). In addition, it is well known that the number of iterations tends to increase with the wavenumber. As shown in fig. 7 (right), for Helmholtz problems, both the GMRES iteration count and the PIBNet prediction errors exhibit a similar correlation with the problem’s wavenumber. In contrast, PIBNet prediction errors and GMRES number of iterations are weakly correlated for Laplace problems which is not a wave problem.

The fig. 8 shows the PIBNet performance per dataset sample with respect to obstacle dispersion. We quantify dispersion as the maximum of the minimum distances between obstacle pairs for each dataset sample. No correlation is observed for any problem. While this is expected for Laplace problems, for wave problems, closely spaced obstacles are anticipated to produce more complex interactions and thus higher errors. Since most of the error is already explained by the wavenumber, one can compute the partial correlation between prediction errors and obstacle dispersion controlled by the wavenumber. This means that the effect of the wavenumber is removed from the correlation between prediction error and obstacle dispersion. We obtain -0.09 and -0.16 for the Helmholtz Dirichlet and the Helmholtz Neumann problems, respectively. The two negative partial correlations between error and obstacle dispersion are consistent with what can be expected from wave problems.

Helmholtz Dirichlet



Helmholtz Neumann



Laplace Dirichlet

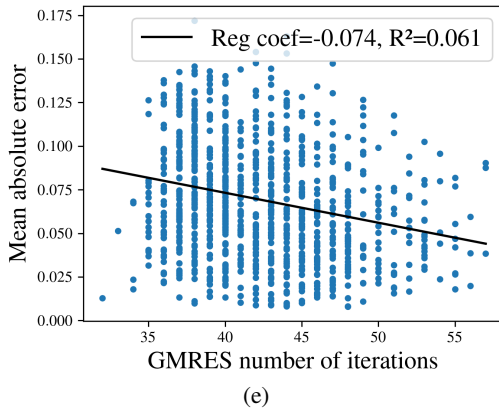


Figure 7: Mean absolute error of PIBNet predictions per dataset sample as a function of GMRES number of iteration to create the corresponding groundtruth (left) and as a function of the corresponding wavenumber (right) for the Helmholtz Dirichlet problem (top), the Helmholtz Neumann problem (middle) and the Laplace Dirichlet problem (bottom).

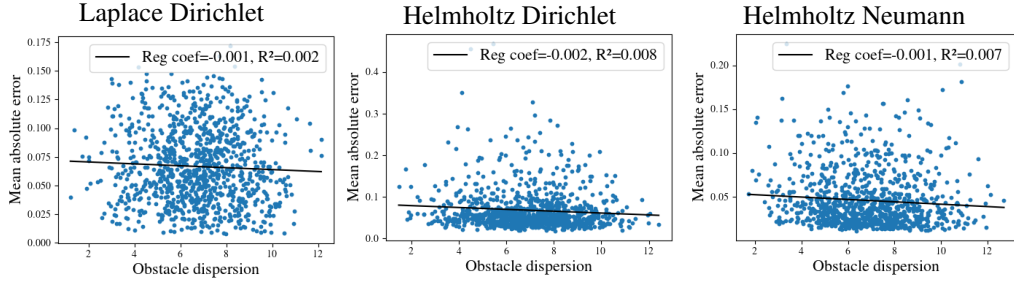


Figure 8: Mean absolute error of PIBNet predictions per dataset sample as a function of obstacle dispersion which is obtained by computing the maximum of the minimum distances between obstacle pairs.

F IMPACT OF THE NUMBER OF CANDIDATE EDGES AT INFERENCE

Figure 9 illustrates the impact on performance of the number of candidate edges n_c per required edge in graph \mathcal{G}^{L-1} when the number of obstacles varies.

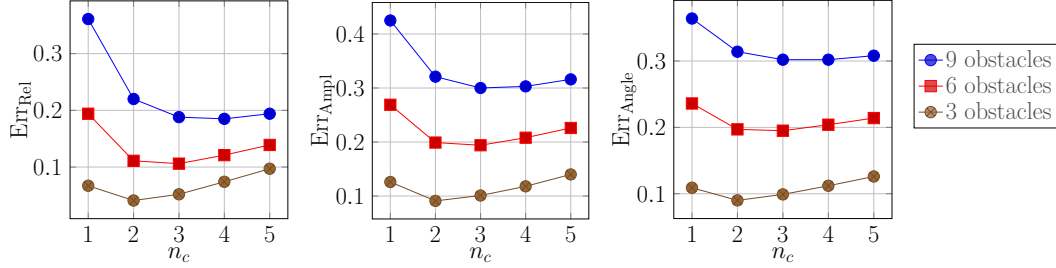


Figure 9: Estimation errors as a function of the number of candidate edges n_c for the Laplace Dirichlet problem (left) and the Helmholtz Dirichlet problem (middle and right).